Materials Advances

ROYAL SOCIETY OF CHEMISTRY

PAPER

View Article Online
View Journal

Cite this: DOI: 10.1039/d6ma00420b

Novel combustion synthesis and spectroscopic investigation of $YInO_3:Cr^{3+}$ polymorphs

Raul Alin Bucur,[a] Alexandra Ioana Bucur,[a] Madalina Ivanovici,[a]
Andrei V. Racu,*[a] Maksym Buryi,[b] Mikhail G. Brik,*[cdefg]
Yevheniia Smortsova,[h] Edgars Vanags,[i] Eugene A. Kotomin[i] and
Vladimir Pankratov*[i]

Received 26th March 2026,
Accepted 26th May 2026

DOI: 10.1039/d6ma00420b

rsc.li/materials-advances

Identifying synthesis pathways for stabilizing metastable phases of materials and understanding the relationship between optical properties and local symmetry are important for advancing optical materials. In this work, we report a novel combustion synthesis route for two polymorphic structures of Cr^{3+}-doped $YInO_3$ perovskite, namely the hexagonal and cubic (C-type) phases, along with their structural and optical properties. The use of tryptophan enabled the stabilization of the less explored metastable C-type $YInO_3$ compound. The structural differences between the polymorphs were identified using X-ray diffraction. Raman spectroscopy confirmed the hexagonal phase through characteristic vibrational bands with peaks at 379 and 611 cm^{-1}, while the predominant band in the C-type phase appears at 386 cm^{-1}. Scanning electron microscopy analysis revealed that the cubic $YInO_3$ polymorph exhibits a smaller grain size compared with the hexagonal phase. Due to the limited crystallographic data available for the cubic phase, its structure was refined using HighScore software, and the corresponding local symmetry parameters were analyzed. Novel excitation and photoluminescence data for $YInO_3:Cr^{3+}$ were obtained in near-infrared (NIR) spectral regions. The Cr^{3+} NIR emission observed at 921 nm in the hexagonal phase is blue-shifted relative to the cubic phase, where the emission maximum occurs at 938 nm. This difference of 17 nm could be correlated with structural difference in local symmetry, such as polyhedral volume $\Delta_{\text{Cub-Hex}}$ 4.1926–5.1527 Å^3. Supplementary visible absorption/excitation, emission, and theoretical calculations of Cr^{3+} energy levels, particularly for the hexagonal phase, were done, and excitation/emission mapping under VUV to elucidate the contribution of potential defects is discussed.

Introduction

The increasing demand for efficient and tunable optical materials has motivated extensive research on oxide-based phosphors and functional ceramic materials. Among these, metastable and low-symmetry crystalline phases have attracted particular interest due to their unique structure–property relationships, which often give rise to novel optical phenomena. In particular, metastable oxide phases with reduced or altered local symmetry represent a rapidly expanding class of functional materials, offering optical properties that cannot be accessed in their thermodynamically stable counterparts. In such systems, subtle changes in coordination geometry and crystal-field strength may drastically modify electronic transitions of optically active dopants, particularly transition-metal ions with strong electron–lattice coupling. Establishing reliable synthesis routes for such materials, along with a fundamental understanding of how crystal chemistry influences their optical response, remains a key challenge in materials science.

---

[a] National Institute of Research and Development for Electrochemistry and Condensed Matter, INCEMC, 144 Str. Prof. Dr A. P. Podeanu, Timisoara, Romania. E-mail: andrei.racu@incemc.ro
[b] Institute of Plasma Physics of the Czech Academy of Sciences, U Slovanky 2525/1a, 182 00 Prague, Czech Republic
[c] School of Integrated Circuits & CQUPT-BUL Innovation Institute, Chongqing University of Posts and Telecommunications, Chongqing 400065, People's Republic of China. E-mail: mikhail.brik@ut.ee
[d] Centre of Excellence for Photoconversion, Vinča Institute of Nuclear Sciences - National Institute of the Republic of Serbia, University of Belgrade, Belgrade, Serbia
[e] Institute of Physics, University of Tartu, W. Ostwald Str. 1, Tartu 50411, Estonia
[f] Faculty of Science and Technology, Jan Długosz University, 42200 Częstochowa, Poland
[g] Academy of Romanian Scientists, 3 Ilfov, 050044, Bucharest, Romania
[h] Deutsches Elektronen-Synchrotron DESY, Notkestr. 85, 22607 Hamburg, Germany
[i] Institute of Solid State Physics, University of Latvia, 8 Kengaraga Str., LV-1063 Riga, Latvia. E-mail: vladimirs.pankratovs@cfi.lu.lv

Perovskite crystals constitute a large group of solids with various crystal structures, including cubic, orthorhombic, monoclinic and other space groups. Their general chemical formula can be written as ABO_3, where A and B can be either two trivalent cations or a divalent and a tetravalent cation, respectively. Such compounds can be easily doped with various transition metal and rare earth ions and can find numerous applications in lighting, sensing, *etc.*

Within oxide-based phosphors, a distinct subcategory is represented by metastable perovskite oxides. Their intrinsic structural characteristics often involve unusual atomic configurations and structurally integrated defects, including lattice distortions associated with local symmetry breaking (*e.g.*, octahedral tilting, bond-angle variations, and bond-length asymmetry within the BO_6 framework), a high concentration of oxygen vacancies and interface-induced structural modifications. Metastable perovskite structures are characterized by non-equilibrium, high-energy states which, compared with thermodynamically stable phases, provide greater structural diversity and consequently enable tunable and optimized functional properties. The non-equilibrium nature of metastable systems requires synthesis through non-equilibrium pathways, typically involving controlled or energetically demanding processing conditions. Under such conditions, the metastable phase can become kinetically trapped, preventing transformation into the thermodynamically stable phase.[1] By carefully tailoring synthesis parameters, various synthesis techniques can be employed to prepare these materials. In particular, high-energy synthesis routes such as pulsed laser deposition, sputtering, high-pressure methods, and combustion synthesis are inherently suitable strategies, as the large amount of energy introduced into the system can stabilize metastable phases and make them energetically competitive with their equilibrium counterparts.[1–3]

Within this framework, $YInO_3$ represents a versatile system, as it can be stabilized in crystallographically distinct hexagonal and cubic polymorphs while preserving an identical chemical composition. Under specific synthesis conditions, some of the perovskites could also adopt a metastable phase, where stability and structure of non-centrosymmetric hexagonal phases transform to a cubic C-type structure, as in the case of some $RInO_3$ (R, rare-earth elements), including $HoInO_3$ and $YInO_3$.[4,5] This polymorphism enables a direct comparison of optical properties governed primarily by differences in local coordination geometry and site symmetry. Several perovskites, such as $RGaO_3$ and $RInO_3$, can adopt either a high-symmetry *P*63/*mmc* phase or a low-symmetry *P*63*cm* phase, with minor differences in their XRD patterns. Despite this, doping strategies and dopants as probes allow the establishment of correlations between local symmetry and optical properties. These techniques, as in the case of photoluminescence, are sensitive enough and may provide valuable insights into the evolution of local structure environments.[6]

The luminescence properties of Cr^{3+} ion in various host materials and the influence of the crystal field on optical properties have been previously discussed in a number of publications.[7,8] Despite extensive studies on the Cr^{3+}-activated luminescence in oxide hosts, most reports focus on thermodynamically stable crystal structures and excitation in the visible or near-ultraviolet range. The combined influence of metastable crystal phases, reduced or unusual coordination environments, and surface-localized Cr^{3+} centers, particularly under high-energy UV/VUV excitation, remains largely unexplored. Addressing this gap is essential for understanding how local symmetry and excitation pathways jointly govern luminescence mechanisms in Cr^{3+}-doped oxides. Understanding the optical behavior of Cr^{3+} ion as a dopant in $YInO_3$ materials and mostly their hexagonal and other stable or metastable phases is essential, taking into consideration the versatility of structure for the emission and absorption properties and their correlations with local symmetry characteristics.[5,9] The emission characteristics of Cr^{3+} in an unusual five-fold coordinated local environment have been analyzed, but in a different oxide system.[10] Under specific combustion synthesis conditions, the orthorhombic phase of $YInO_3$ was obtained and doped with Cr^{3+} ions.[9]

However, the derived structure of the cubic C-type $YInO_3$ polymorph may exhibit similarities in local symmetries with cubic Sc_2O_3 (or In_2O_3) oxides, which have also been studied as Cr^{3+} doped systems.[11,12] Other solid solutions of indates like $YIn_{1-x}Fe_xO_3$, $YMn_{1-x}In_xO_3$, $Y_{1-x}Gd_xInO_3$, and Eu^{3+} doped $YInO_3$ with metastable C-type were partially studied.[5,13–16] It is worth noting that structural modifications in the $YMn_{1-x}In_xO_3$ solid solutions, analyzed using Raman spectroscopy, have highlighted peaks in the 350–450 cm^{-1} range, distinguishing the hexagonal and cubic phases[17] Other perovskites investigations include experimental and density functional theory (DFT) studies on the electronic structures of $LnInO_3$ (Ln = La, Pr, Nd, Sm) or (Dy, Er, Ho).[18,19] Furthermore, the compounds $XInO_3$ (X – Rb, Cs, Fr) with a cubic structure, along with their electronic properties, have also been explored by first-principles DFT-based calculations.[20] DFT calculations have also been conducted to further understand some optoelectronic and thermoelectric properties and the cubic structure of $YInO_3$ or $GaInO_3$.[21] Despite these extensive studies, the correlation between synthesis conditions, phase stabilization and the resulting local symmetry around Cr^{3+} ions in perovskite-derived systems remains an open area of investigation. In particular, exploring non-equilibrium synthesis approaches that enable access to metastable structures offers new opportunities to tailor optical properties. Therefore, a systematic examination of Cr^{3+} doped perovskite materials with controlled symmetry environments can provide valuable insights into structure–luminescence relationships and support the design of next generation optical and multifunctional materials.

Thus, in order to establish a direct correlation between crystal structure, local symmetry, and optical response, a set of complementary experimental techniques should be intentionally combined. X-ray diffraction provides phase identification and average crystallographic symmetry, while Raman spectroscopy probes local structural distortions and phase-related vibrational fingerprints. Scanning electron microscopy yields information on morphology and particle size, which is essential for understanding surface-related optical effects. Photoluminescence spectroscopy under visible excitation selectively probes bulk Cr^{3+} centers, whereas synchrotron-based UV/VUV excitation enables access to surface-dominated and host-mediated excitation pathways. Finally, crystal-field analysis within the Tanabe–Sugano framework allows quantitative interpretation of the experimental spectra in terms of local coordination and symmetry.

Therefore, in this work, we report an adapted and unique gel-combustion synthesis route that enables the selective stabilization of hexagonal and metastable cubic C-type $YInO_3:Cr^{3+}$ polymorphs. The main objectives are: (i) to elucidate a novel combustion synthesis approach for obtaining the metastable C-type $YInO_3:Cr^{3+}$ phase; (ii) to correlate differences in structure, local coordination symmetry, and optical properties of Cr^{3+} ions in both polymorphs; and (iii) to interpret, using data provided in the SI, the hexagonal phase visible-range spectroscopy, Cr^{3+} energy level calculations, and VUV excitation–emission mapping, analyzing contributions from potential defects or impurities.

Materials and methods

Hexagonal and cubic samples of $YIn_{1-x}Cr_xO_3$ ($x = 0.005$) were prepared by a novel combustion method in air. The reagents used were: $Y(NO_3)_3{\cdot}4H_2O$ (Sigma Aldrich), metallic indium, HNO_3 (69%, ρ = 1,41 g cm^{-3}, Merck KGaA), $Cr(NO_3)_3{\cdot}9H_2O$ (Sigma Aldrich), NH_3 (25%, Chimreactiv SRL), Leucine (AppliChem GmbH) and Tryptophan (AppliChem GmbH). The precursor solutions for both cubic and hexagonal samples were: indium nitrate with concentrations of 1 mol L^{-1} for $YInO_3$, and 0.995 mol L^{-1} for $YIn_{1-x}Cr_xO_3$, respectively, yttrium nitrate of concentration 1 mol L^{-1} and chromium nitrate of concentration 0.005 mol L^{-1}. Indium nitrate solutions were obtained by dissolving appropriate amounts of metallic indium in HNO_3. In order to obtain samples with hexagonal crystallographic symmetry, 300 μL of precursors were mixed in an alumina crucible and left in air for 1 hour for better diffusion. Subsequently, to each composition, 0.39 g of Leucine and 900 μL of NH_3 were added. The as prepared samples were heated in air at 1120 °C for 1 hour, with a heating rate of 5° per min, then naturally cooled to room temperature. In order to obtain samples with cubic crystallographic symmetry, 300 μL of precursors were mixed on a watch glass, and left in the air for 1 hour for better diffusion. Subsequently, to each composition, 300 μL of HNO_3 and 0.0876 g of Tryptophan were added. The gel obtained was placed on a hot plate and heated freely up to approximately 300 °C. As soon as the gel is dry, a blowtorch is used to initiate the combustion reaction. The resulting powders were ground and transferred to an alumina crucible. Finally, the samples were heated in air at 1250 °C for 1 hour, with a heating rate of 10° per min, then naturally cooled to room temperature.

The crystalline structure of the samples was examined by long-time X-ray diffraction using a PanAnalytical X'Pert Pro MPD diffractometer PW (Netherlands) with CuKα radiation, at room temperature. The Rietveld refinement was performed using a pseudo-Voigt profile function and the X'Pert HighScore Plus software (PANalytical).[22] The Endeavour software by H. Putz and K. Brandenburg (Crystal Impact, Germany) was used for crystal structure solution based on XRD patterns, unit-cell parameters and chemical composition data.[23] The program employs a direct-space global optimization approach, using simulated annealing and Monte Carlo algorithms to explore possible atomic arrangements. The resulting structural models, which achieve an R-factor of up to 20%, are considered optimal for solutions obtained from powder diffraction data.

Raman spectroscopy measurements were carried out using a μRaman module (Nanonics Imaging Ltd., Israel) coupled with a Shamrock 500i spectrograph (ANDOR, UK). The measurements were taken at room temperature with a 50x objective, employing a 514.5 nm laser as the excitation source and an exposure time of 20 seconds. The room temperature photoluminescence measurements in the UV-VIS domain were performed using the FLS 980, Edinburgh Instruments spectrometer. A Xe lamp was used as the excitation source, and for a typical scan, the monochromator slits for both excitation and emission were set to 1 nm. The PMT Hamamatsu R928P detector was used. Photoluminescence experiments under ultraviolet (UV) and vacuum ultraviolet (VUV) excitation were carried out at the P66 beamline of the PETRA III storage ring at DESY (the beamline and the SUPERLUMI end station).[24,25] The excitation radiation at P66 is generated by a bending magnet source and is therefore relatively moderate, not inducing radiation-related defects in the studied samples. The corresponding photon flux is approximately two orders of magnitude lower than that at the undulator-based FinEstBeAMS beamline[26–28] of the MAX IV synchrotron, to avoid radiation damage due to the high excitation intensity.

Microstructural and compositional analyses were performed using a Helios 5 UX scanning electron microscope (Thermo Fisher Scientific, Netherlands). For image acquisition, the powder samples were prepared by lightly distributing the powders onto a conductive carbon tape and removing unbound particles with a controlled nitrogen stream. To acquire micrographs, the microscope was operated in immersion mode at 2 kV and 13 pA using a through-the-lens detector (TLD) and a short-dwell multi-frame acquisition scheme (50 ns dwell, 30-frame integration) to suppress charging in the insulating oxide powders. For quantitative energy-dispersive X-ray spectroscopy (EDX), the measurements were performed on 5 mm pellets pressed at 2 tons using a Specac Atlas 15T hydraulic press. The pellets were then coated with a thin carbon film using a Quorum Q150R ES Plus sputter coater (UK; 3 pulses, 35 A, 30 s intervals, 4×10^{-2} Pa) and the EDX spectra were acquired at 20 kV with a 60 s live time. Quantitative analysis was performed using PathFinder 2.8 software (Thermo Fisher Scientific, USA). To calculate the Cr^{3+} energy levels in this work, we used a simplified approach, using equations derived from the Tanabe-Sugano matrices for the energy levels of the d^3 electron configuration – $E(^4T_{2g})$, $E(^4T_{1g}(^4F))$, and $E(^2E_g)$ of the $^4T_{2g}$, $^4T_{1g}(^4F)$, and ^2E_g states.[29]

Results and discussion

Structure analysis

The crystalline phase formation and structural evolution of $YInO_3$ are strongly influenced by synthesis parameters, particularly the choice of chelating agents in combustion synthesis. Variations in the combustion chemistry can modify reaction kinetics, local temperature profiles and cation diffusion, thereby stabilizing distinct crystal structures. To elucidate these effects, X-ray diffraction analysis was employed to examine the phase composition and structural characteristics of $YInO_3$ powders synthesized under different chelation conditions. It is worth emphasizing that the final powders were prepared using two distinct combustion synthesis routes, each employing a different amino acid—Leucine or Tryptophan. These compounds are regarded as novel fuels in combustion synthesis and only limited studies have documented their utilization, particularly that of Tryptophan.[30–33] In this study, the amino acids served a dual function, acting as chelating agents during the gel formation stage and as fuels in the combustion stage. Moreover, the combustion stage and the thermal treatment were carried out using different approaches.

The XRD patterns of the calcined powders obtained using leucine as a chelating agent (Fig. 1a and b) reveal the formation of the hexagonal crystalline $YInO_3$ phase, identified according to the ICDD reference 01-070-0122 (Fig. 1d), corresponding to the space group *P63cm*. Due to the highly exothermic and rapid reaction inherent to combustion synthesis, a minor secondary phase, of cubic C-type $YInO_3$ (indicated by red arrows), is also observed in all hexagonal samples. The hexagonal structure is characterized by long-range ordering of Y^{3+} and In^{3+} cations, which is favored under conditions of high local temperature and sufficient cation diffusion.

In contrast, when tryptophan is used as the chelating agent, the powders exhibit the cubic C-type bixbyite structure of $YInO_3$, corresponding to ICDD reference 00-025-1172 and crystallizing in the $Ia\bar{3}$ space group (Fig. 1d). This cubic structure, with composition $(Y_{0.5}In_{0.5})_2O_3$, features random occupancy of Y^{3+} and In^{3+} cations across the two crystallographically distinct sites, resulting in complete cation disorder. The diffraction peak indicated by the black arrow may correspond to the (123)/(213) reflection characteristic of the cubic phase or traces of minor hexagonal $YInO_3$.

Unlike the hexagonal phase, which is thermodynamically stable at ambient conditions, the cubic C-type phase is metastable and typically forms under non-equilibrium conditions, converting to the hexagonal phase upon sufficient thermal treatment (~1175–1250 °C), as reported in previous studies.[34]

The observed phase selectivity can be rationalized by differences in the molecular structure, combustion behavior and coordination chemistry of the chelating agents. Leucine is a small aliphatic amino acid with relatively simple coordination ability and a thermal decomposition activation energy of approximately 160 kJ mol^{-1}.

Its combustion is rapid and highly exothermic (heat of combustion ≈27.3 kJ g^{-1}), generating higher local temperatures

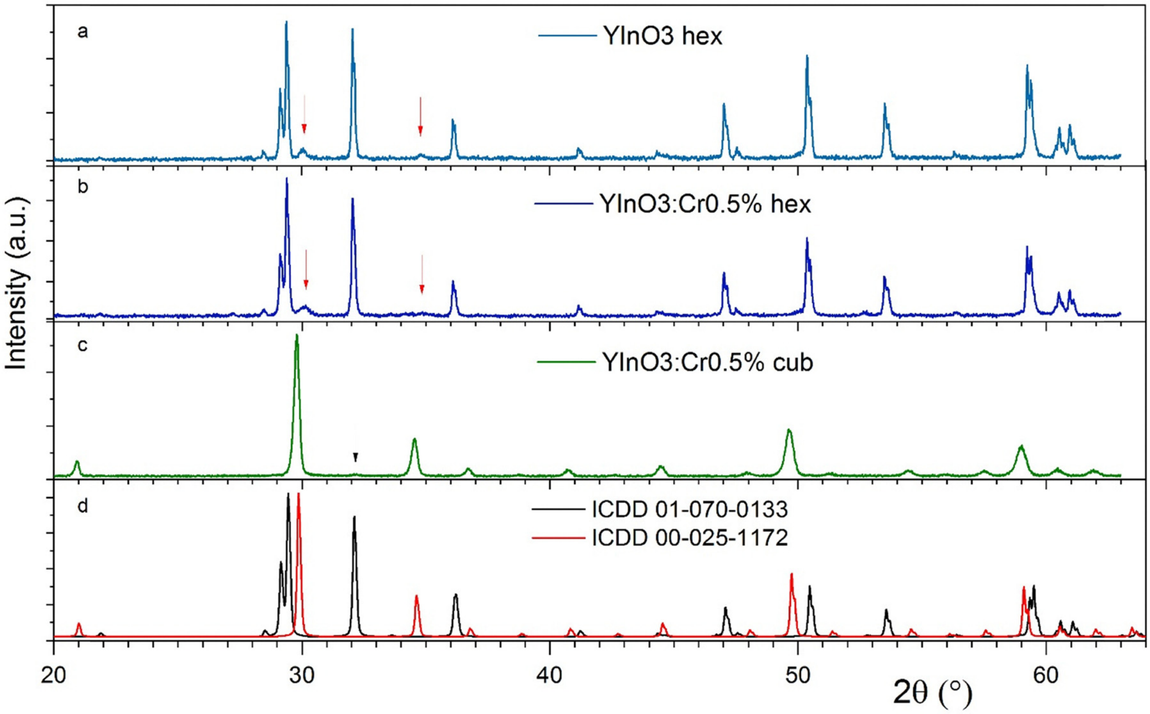

Fig. 1 X-ray diffraction patterns of hexagonal (a) and (b) and C-type $YInO_3$ (c), correlated with ICDD reference data (d).

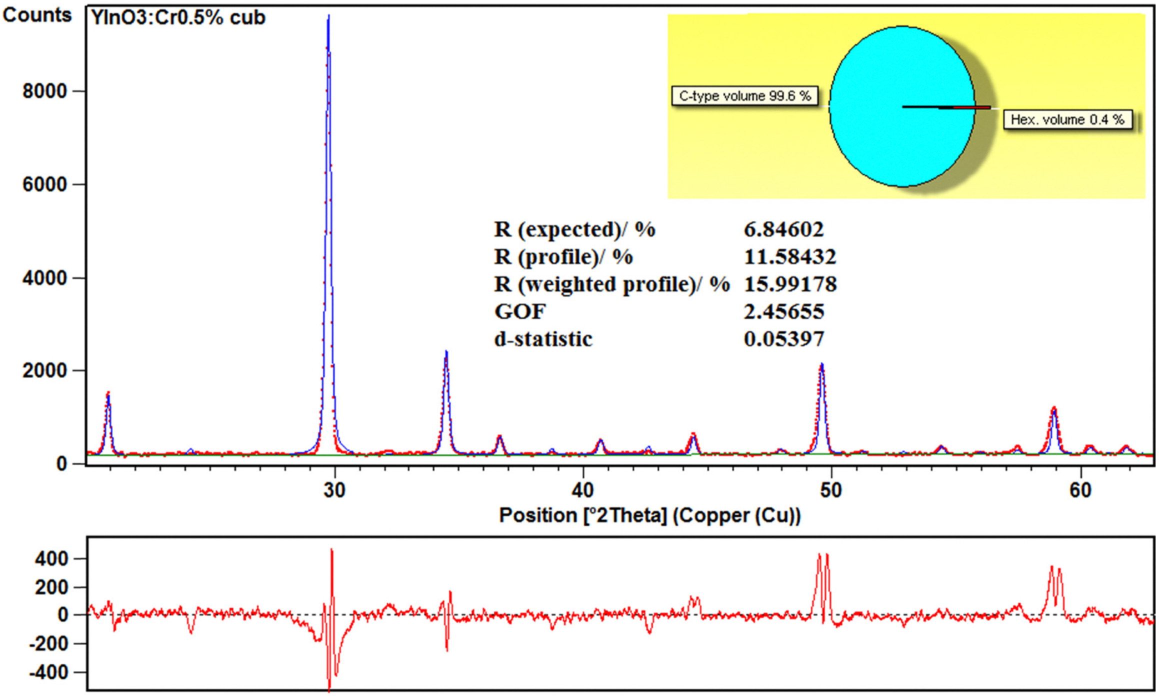

Fig. 2 HighScore Rietveld refinement of Cr^{3+}-doped C-type $YInO_3$.

that favor cation ordering and the formation of the thermodynamically stable hexagonal $YInO_3$. In contrast, tryptophan contains a bulky aromatic indole group, exhibits a slightly higher heat of combustion ($\approx$31.0 kJ g^{-1}) and has a significantly higher decomposition activation energy ($\approx$195 kJ mol^{-1}). This higher energy barrier for decomposition, combined with the structural complexity of the indole ring, results in a distinct combustion kinetic profile characterized by enhanced gas evolution. The substantial variation in activation energy critically influences both the ignition characteristics and the combustion mode, thereby affecting the thermal evolution of the system. This environment suppresses long-range cation ordering and favors retention of the metastable cubic C-type phase. The indole ring further enhances coordination with metal cations, which increases steric hindrance and contributes to kinetic stabilization of the cubic structure. These findings highlight the microscopic role of chelating agents in regulating phase formation in $YInO_3$. The combination of thermochemical properties, molecular structure and combustion kinetics explains why leucine promotes the ordered hexagonal phase, whereas tryptophan stabilizes the metastable cubic C-type structure. Rapid nucleation, limited cation diffusion and enhanced gas evolution in tryptophan-assisted combustion collectively prevent the system from reaching the equilibrium hexagonal configuration, providing a mechanistic understanding of the experimentally observed phase selectivity.

Rietveld refinement has been performed using XDR HighScore software. The refinement pattern results for C-type $YInO_3$:Cr^{3+} are shown in Fig. 2 and for the hexagonal phase in SI Fig. S1. The determined structural parameters are listed in Table 1.

The SEM measurements were performed to characterize the morphology of $YInO_3$:Cr^{3+} samples. Fig. 3 displays the surface morphology of all samples, along with EDAX measurements, which prove that within the error margins of the electron microscope, the anticipated compositions were obtained. In the case of cubic $YInO_3$:0.5% Cr, the use of the combustion synthesis with Tryptophan resulted in reduced crystallite size (around 200 nm), as the highly exothermic and short-duration reaction promotes rapid nucleation and limits grain growth.

The combustion synthesis technique also promotes rapid gas evolution and fast reaction kinetics, resulting in a highly porous crystalline network with relatively large pore sizes. Moreover, it can be noticed that the C-type particles exhibit a spherical prolonged shape and a more uniform morphology.

Table 1 Structural refinement results for $YInO_3$ polymorphs

Compound	Space group (No.)	a (Å)	b (Å)	c (Å)	V (10^6 pm^3)	α, γ angles
$YInO_3$ hex	*P63cm* (185)	6.2716 (6)	6.2716 (6)	12.254 (1)	417.4258	90° 120°
$YInO_3$:Cr0.5% hex	*P63cm* (185)	6.273 (1)	6.273 (1)	12.256 (2)	417.7448	90° 120°
$YInO_3$:Cr0.5% cub	*Ia*$\bar{3}$ (206)	10.3876 (5)	10.3876 (5)	10.3876 (5)	1120.833	90° 90°

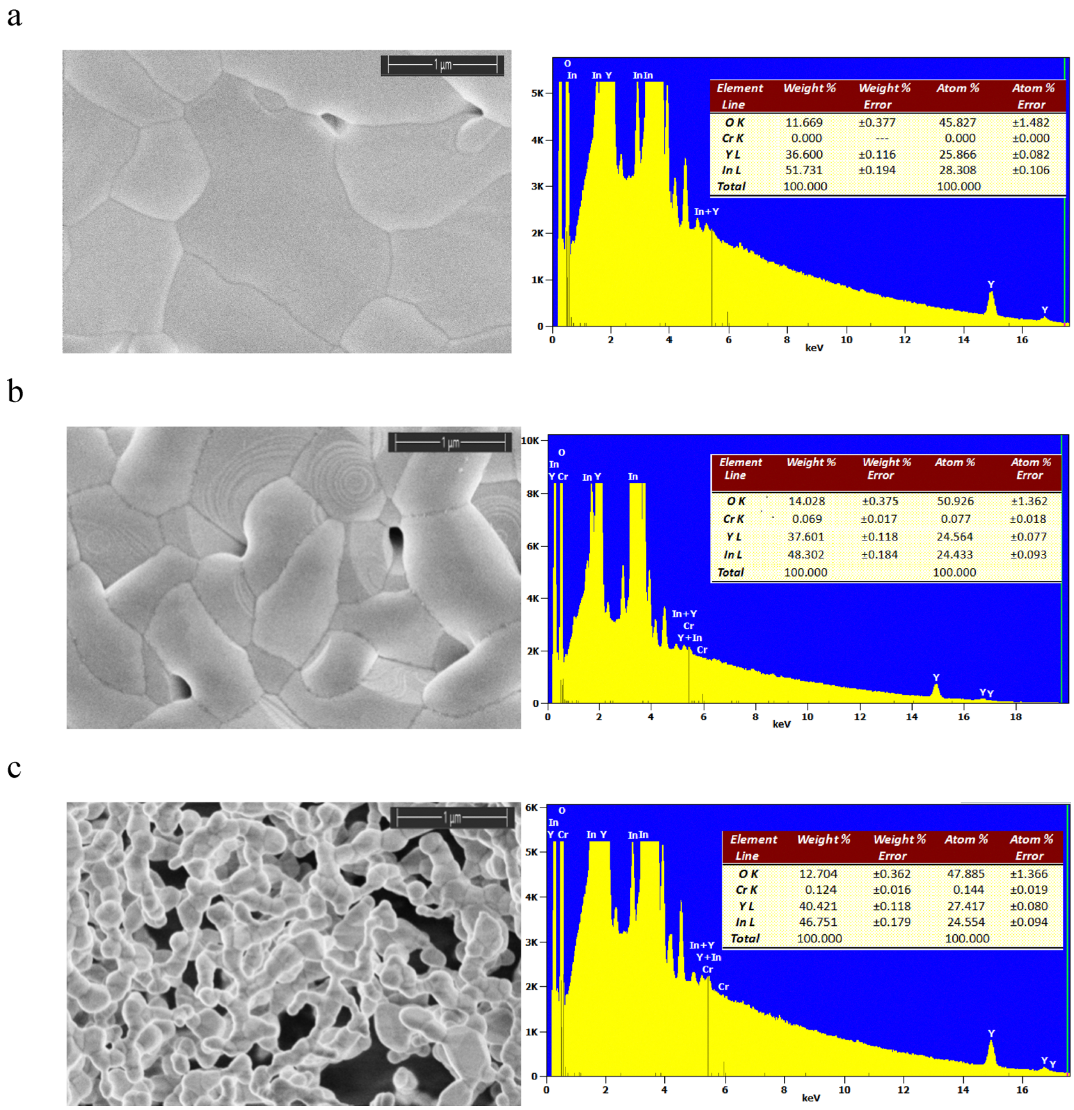

a

Element Line	Weight %	Weight % Error	Atom %	Atom % Error
O K	11.669	±0.377	45.827	±1.482
Cr K	0.000	---	0.000	±0.000
Y L	36.600	±0.116	25.866	±0.082
In L	51.731	±0.194	28.308	±0.106
Total	100.000		100.000	

b

Element Line	Weight %	Weight % Error	Atom %	Atom % Error
O K	14.028	±0.375	50.926	±1.362
Cr K	0.069	±0.017	0.077	±0.018
Y L	37.601	±0.118	24.564	±0.077
In L	48.302	±0.184	24.433	±0.093
Total	100.000		100.000	

c

Element Line	Weight %	Weight % Error	Atom %	Atom % Error
O K	12.704	±0.362	47.885	±1.366
Cr K	0.124	±0.016	0.144	±0.019
Y L	40.421	±0.118	27.417	±0.080
In L	46.751	±0.179	24.554	±0.094
Total	100.000		100.000	

Fig. 3 SEM images and EDAX results for $YInO_3$ hexagonal (a), Cr^{3+}-doped $YInO_3$:0.5% hexagonal (b), and Cr^{3+}-doped $YInO_3$:0.5% cubic (c) phases.

The Raman measurements were performed on a hexagonal and cubic $YInO_3$ samples under 514 nm laser excitation. The registered peaks are listed in Table 2 and Fig. 4.

A good agreement was obtained with published data on a similar hexagonal host reported by N. Arai and other references in Table 2. The observed peak at ~611 cm^{-1} could also be common for the cubic and the hexagonal phases, as confirmed in the reported data.[5]

Table 2 Observed Raman peaks for hexagonal and C-type $YInO_3$ phases

Ref.	Raman shift (cm^{-1})					
This work hex	301	326	364	379	435	611
5	297	323	364	378	431	612
15	300	328	—	381	437	612
16	299	325	364	379	432	611
This work cub		386	461	484	580	610

Additionally, the peak at 402 cm^{-1} is reported by Shukla *et al.*, to be a component of the C-type phase, which in Fig. 3b can be seen as a component of a shoulder with a peak at 386 cm^{-1}.[5]

Local symmetry

The structural properties of the synthesized $YInO_3$ samples were analyzed and compared, showing the difference in local symmetry of the cationic sites. The resulting polyhedra of local symmetry of both phases are shown in Fig. 5. The substitution of Cr^{3+} during doping in hexagonal $YInO_3$ favors occupation of the In^{3+} 6c site with structural parameters shown in Table 3 (row 1). The following observations can be made: the hexagonal $YInO_3$ phase exhibits fivefold coordination at the 6c, In^{3+} site, in contrast, the cubic phase of $YInO_3$ has two six-coordinated sites, 24d and 8a, as shown in Table 3 (row 2). Based on the determined cubic structural model, obtained using the structure-solution tool Endeavour,[23] the In^{3+} cations occupy a single 24d site in the cubic phase, whereas the 8a site is

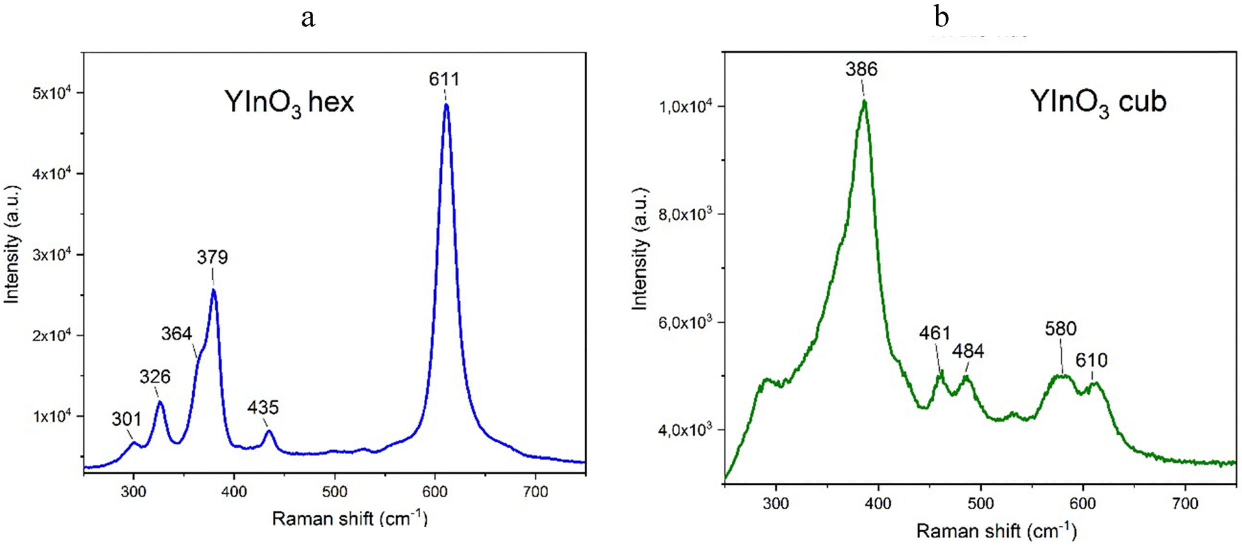

Fig. 4 Raman spectra of the synthesized $YInO_3$ phases: (a) hexagonal and (b) cubic (C-type).

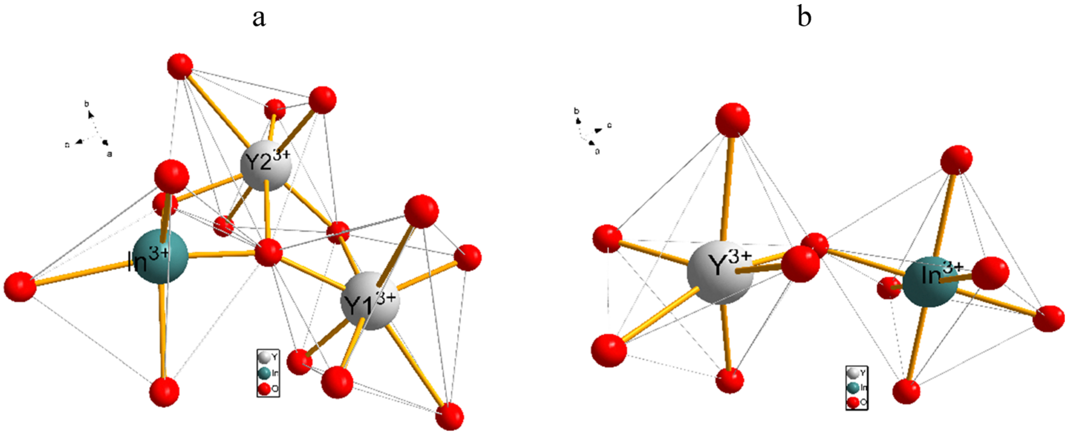

Fig. 5 Local coordination environments in $YInO_3$, (a) hexagonal phase showing InO_5 and two YO_7 polyhedra, and (b) cubic (C-type) phase showing InO_6 and YO_6 polyhedra.

occupied by Y^{3+} ions. The corresponding local polyhedral parameters are presented in Fig. 5 (b) and Table 3.

A comparison of the In^{3+} local environments in the cubic (24d site) and hexagonal (6c site) phases shows an increase in coordination number from 5 to 6, which results also in the increase of 0.0084 Å in the average In–O bond length and expands the polyhedral volume with 4.1926 Å^3 for the C-type 24d site.

However, in the C-type structure, of A_2O_3 type, such as In_2O_3, dopants as Sn^{4+} prefers the 8b site.[35] This could depend on A cation but also on a dopant like in Sc_2O_3:Cr^{3+} prefer mostly C_{3i} symmetry (8a) but in Y_2O_3 host the Cr^{3+} is mentioned to occupy the C_2 site (24d).[11,12,36]

These crystallographic differences directly determine the local coordination and symmetry of the cation sites, which are correlated with optical properties in the following section.

Spectroscopic consideration

Diffuse reflectance spectra of both hexagonal and cubic $YInO_3$ phases were measured and converted using the Kubelka–Munk function to visualize the UV absorption edge of the samples (Fig. 6a). The optical bandgap for the hexagonal phase was determined to be $E_g = 3.63$ eV, while for the cubic phase it was $E_g = 3.63$ eV. Both values were calculated using Tauc plots, as shown in the inset of Fig. 6a.

The use of synchrotron-based UV/VUV radiation enables a substantial extension of the luminescence excitation energy range, beyond the bandgap. Spectroscopy with tunable VUV excitation allows a direct comparison of impurity-centre luminescence under both direct intracentre excitation and excitation mediated by energy transfer from the intrinsic electronic states of the host lattice, including electron–hole pairs, excitons, and defects. This approach is particularly

Table 3 Site symmetries of hexagonal and cubic $YInO_3$ phases, along with those of related cubic oxides

Nr.	Compound	Space group number	Site symbol (Wickoff)	CN	Avg. bond length (Å)	Min. bond length (Å)	Max. bond length (Å)	Polyhedral volume (Å^3)
1	$YInO_3$ (hex), Y0 site	185	4b	7	2.3149	2.07858	2.62456	18.7113
	$YInO_3$ (hex), Y1 site	185	2a	7	2.3719	2.16980	2.62281	19.6016
	$YInO_3$ (hex), In1 site	185	6c	5	2.1608	1.89730	2.33779	8.6172
2	$YInO_3$ (cub), In0 site	206	24d	6	2.1692	2.16925	2.16925	12.8098
	$YInO_3$ (cub), Y0 site	206	8a	6	2.2623	2.16698	2.37320	13.7699
3	In_2O_3 (cub), In0 site[a]	206	24d	6	2.1941	2.14047	2.23125	12.7408
	In_2O_3 (cub), In1 site[a]	206	8b	6	2.1859	2.18590	2.18590	13.3142
4	Y_2O_3 (cub), Y0 site[a]	206	24d	6	2.2838	2.26972	2.24709	14.2879
	Y_2O_3 (cub), Y1 site[a]	206	8a	6	2.2841	2.28413	2.28413	15.0069
5	Sc_2O_3(cub), Sc0 site[a]	206	24d	6	2.1260	2.08750	2.16696	11.6201
	Sc_2O_3 (cub), Sc1 site[a]	206	8a	6	2.1234	2.12344	2.12344	12.2046

[a] Data from materials project crystallographic files repository. CN stays for coordination number.

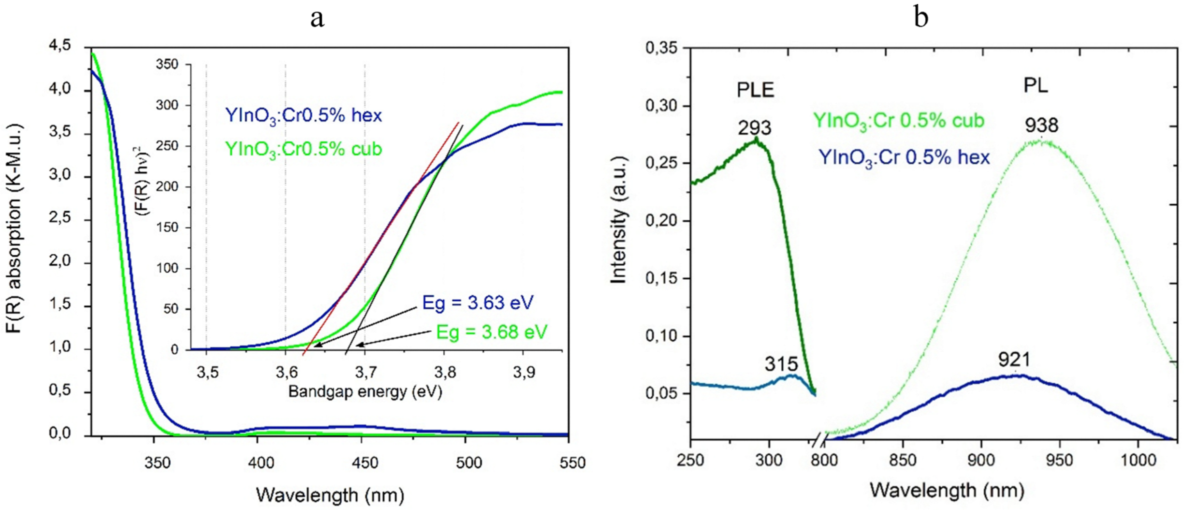

Fig. 6 (a) Kubelka–Munk absorption spectra and the corresponding bandgap determination (inset) for Cr^{3+}-doped hexagonal and cubic $YInO_3$ phases. (b) Photoluminescence excitation in the UV region and Cr^{3+} NIR emission of the samples.

important for wide-bandgap materials,[37–47] including perovskites.[48,49]

Fig. 6b presents the photoluminescence excitation and emission results obtained for $YInO_3$:Cr^{3+}(0.5%) with hexagonal and cubic crystal structures. Under UV/VUV excitation, all doped samples exhibited broad luminescence bands in the near-infrared spectral range. It can be observed that the emission at 921 nm in the hexagonal phase is blue shifted compared with the cubic phase 938 nm emission, being attributed to Cr^{3+} dopant emission. Comparing with cubic Sc_2O_3:Cr, the emission in NIR at 870 nm is substantially blue shifted, possibly due to Cr^{3+} preference mostly of C_{3i} symmetry (8a) in this host.[11]

Because the absorption coefficient of $YInO_3$ above 3.6 eV is extremely high, the penetration depth becomes very small, meaning that the excitation is localized almost entirely within the near-surface region of the particles. The Cr^{3+} ions at or near the surface experience reduced coordination, lower crystal-field strength, and enhanced structural disorder compared to bulk Cr^{3+} sites.

According to the Tanabe–Sugano diagram, these surface environments correspond to a deeper weak-field regime in which the $^4T_2$ level lies below or very close to ^2E. In this case, relaxation into the ^2E state becomes highly inefficient, and the population remains in the vibronically active $^4T_2$ manifold. Radiative decay $^4T_2 \rightarrow {}^4A_2$ therefore becomes dominant and produces the broad, featureless NIR band centered at 900–950 nm, as seen in Fig. 6b.

Importantly, the observed emission band at 920–940 nm falls well within the characteristic NIR range of Cr^{3+} broadband emission ($^4T_2 \rightarrow {}^4A_2$) in weak crystal fields. In contrast, Cr^{4+} centers in oxide hosts are known to exhibit broadband emission predominantly in the longer-wavelength NIR region (typically above 1100 nm and often peaking near 1200 nm), accompanied by distinct excitation and absorption features in the visible–NIR range.[50,51] The absence of any pronounced emission beyond 1100 nm, as well as the lack of characteristic Cr^{4+}-related excitation signatures, makes a significant contribution from Cr^{4+} centers unlikely.

Supplementary aspects related to visible absorption/excitation, emission, and theoretical calculations of Cr^{3+} energy levels, particularly for the hexagonal phase, are detailed in

Table 4 Correlation between structural characteristics and optical properties

Nr.	Compound	Space group number	Site symbol (Wickoff)	CN	Avg. bond (Å)	Polyh. volume (Å^3)	Bandgap (eV)	PLE (nm)	PL (nm)
1	YInO$_3$ (hex), In1 site	185	6c	5	2.1608	8.6172	3.63	315	921
2	YInO$_3$ (cub), In0 site	206	24d	6	2.1692	12.8098	3.68	293	938
	YInO$_3$ (cub), Y0 site		8a		2.2623	13.7699			

the (SI), Chapter 2. Additionally, excitation/emission mapping under VUV excitation and the contribution of potential defects are discussed in Chapter 3.

Differences in the structure of Cr-doped YInO$_3$ between the hexagonal and cubic phases influence the local symmetry, including variations in polyhedral volume ($_{\text{Cub-Hex}}$ 4.1926–5.1527 Å^3) and consequently lead to differences in optical properties, such as an emission maximum shift of approximately 17 nm, as shown in Table 4.

Conclusions

In this study, we successfully synthesized and investigated the optical properties of Cr^{3+}-doped YInO$_3$ perovskite powders. A novel combustion method was developed to obtain both the cubic and hexagonal phases. A gel-combustion synthesis employing tryptophan enabled the stabilization of the less explored metastable C-type YInO$_3$ phase. The study demonstrates that the choice of chelating agent governs the phase selectivity in YInO$_3$, with leucine favoring the thermodynamically stable hexagonal structure and tryptophan stabilizing the metastable cubic C-type phase through differences in combustion kinetics, thermal decomposition and cation mobility. Both structural polymorphs were confirmed by XRD. Raman spectroscopy confirmed the hexagonal phase through characteristic vibrational bands with peaks at 379 and 611 cm^{-1}, while in C-type prevail band has a 386 cm^{-1} peak. SEM imaging indicated that the cubic YInO$_3$ phase exhibits a smaller grain size than the hexagonal one. Owing to the limited crystallographic data available for the cubic phase its structure was refined and further analyzed in terms of local symmetry and coordination environments. Importantly, near-infrared photoluminescence showed a clear dependence on crystal structure: the emission maximum at 921 nm for the hexagonal phase is blue-shifted relative to 938 nm for the cubic phase. This ∼17 nm shift is correlated with differences in local symmetry and polyhedral volume $_{\text{Cub-Hex}}$ 4.1926–5.1527 Å^3, highlighting the strong relationship between structural characteristics and optical properties. Supplementary visible absorption/excitation and emission measurements, along with theoretical calculations of Cr^{3+} energy levels, especially for the hexagonal phase were conducted. Furthermore, excitation/emission mapping under VUV irradiation was performed to clarify the role of potential defects. These findings contribute to a deeper understanding of the optical properties and structure–property relationships of Cr^{3+}-doped YInO$_3$ polymorphs and demonstrate the potential of combustion synthesis for obtaining metastable phases, providing valuable insights for their application in optoelectronic materials.

Author contributions

R. A. B: methodology, investigation, writing – original draft, writing – review & editing, resources. A. I. B: investigation, writing – review & editing, formal analysis, resources. M. I: formal analysis, writing – review & editing, resources. A. V. R: conceptualization, investigation, writing – original draft, writing – review & editing. M. B: writing – review & editing investigation, formal analysis. M. G. B: conceptualization, investigation, writing – original draft, writing – review & editing, validation. Y. S.: investigation, formal analysis, writing – review & editing. E. V: formal analysis, investigation. E. A. K: investigation, formal analysis, resources. V. P: methodology, conceptualization, investigation, writing – original draft, writing – review & editing.

Conflicts of interest

There are no conflicts to declare.

Data availability

The data that support the findings of this study are available from the corresponding author upon reasonable request.

Visible absorption/excitation, emission, and theoretical calculations of Cr^{3+} energy levels, particularly for the hexagonal phase, as well as excitation/emission mapping under VUV to elucidate the contribution of potential defects, are presented in the supplementary information (SI). See DOI: https://doi.org/10.1039/d6ma00420b.

Acknowledgements

M. G. B. thanks the National Science Center (NCN) Poland under project no. 2023/49/B/ST5/03384; Ministry of Science, Technological Development, and Innovation of the Republic of Serbia under contract 451-03-47/2023-01/200017; Program for the Foreign Experts (Grant No. W2017011) offered by Chongqing University of Posts and Telecommunications; The National Foreign Experts Program for ''Belt and Road Initiative'' Innovative Talent Exchange (Grant No. DL2021035001L); Estonian Research Council grant PRG2031; E. A. K and V. P acknowledges LZP grant 2023/1-0063 for the support; Nucleu Program within the National Research Development and Innovation Plan 2022–2027, with the support of MCID, project no

PN 23 27 02 01, contract no. 29N/2023; A. V. R, M. I., M. G. B. acknowledge the support of Romania's National Recovery and Resilience Plan – NRRP (PNRR), Project C9-I8-C28, and Contract 760107/2023; We acknowledge DESY (Hamburg, Germany), a member of the Helmholtz Association HGF, for the provision of experimental facilities. This research was carried out at P66 beamline at PETRA III and we would like to thank Aleksei Kotlov for his assistance in using of SUPERLUMI setup. Beamtime was allocated for proposal I-20250639 EC

References

1 Y. Feng, J. Dai, M. Wang, W. Ding, H. Zhang, W. Xu and J. Wan, *Microstructures*, 2025, **5**, 2025068.

2 H. Gyulasaryan, A. Kuzanyan, A. Manukyan and A. S. Mukasyan, *Nanomaterials*, 2023, **13**, 1902.

3 V. Kocevski, J. A. Valdez, B. K. Derby, Y. Q. Wang, G. Pilania and B. P. Uberuaga, *Mater. Adv.*, 2023, **4**, 1101–1112.

4 C. W. F. T. Pistorius and G. J. Kruger, *J. Inorg. Nucl. Chem.*, 1976, **38**, 1471–1475.

5 R. Shukla, S. Gupta, V. Grover, V. Natarajan and A. Tyagi, *Dalton Trans.*, 2014, **44**, 10628–10635.

6 A. V. Racu, Z. Ristić, A. Ćirić, V. Đorđević, G. Buşe, M. Poienar, M. J. Gutmann, O. Ivashko, M. Ştef, D. Vizman, M. D. Dramićanin, M. Piasecki and M. G. Brik, *Opt. Mater.*, 2023, **136**, 113337.

7 G. Wei, P. Li, R. Li, Y. Wang, S. He, J. Li, Y. Shi, H. Suo, Y. Yang and Z. Wang, *Adv. Opt. Mater.*, 2023, **11**, 2301794.

8 F. Zhao, Z. Song and Q. Liu, *Laser Photonics Rev.*, 2022, **16**, 2200380.

9 K. Naveen, N. Kumar, T. K. Mandal, P. D. Babu, V. Siruguri, P. K. Maji and A. K. Paul, *J. Mol. Struct.*, 2019, **1185**, 432–439.

10 S. Li, J. Wu, R. Li, Z. Zhang, Z. Qiu, Y. Liu and S. Lian, *Ceram. Interfaces*, 2023, **49**, 14581–14586.

11 S. Kück, L. Fornasiero, E. Mix and G. Huber, *J. Lumin.*, 2000, **87–89**, 1122–1125.

12 V. Lupei, A. Lupei, A. Ikesue and S. Florea, in *CLEO/Europe - EQEC 2009 - European Conference on Lasers and Electro-Optics and the European Quantum Electronics Conference*, IEEE, Munich, Germany, 2009, p. CA_P17.

13 Y. F. Gomes, J. Li, K. F. Silva, A. A. G. Santiago, M. R. D. Bomio, C. A. Paskocimas, M. A. Subramanian and F. V. Motta, *Ceram. Int.*, 2018, **44**, 11932–11939.

14 A. E. Smith, M. C. Comstock and M. A. Subramanian, *Dyes Pigm.*, 2016, **133**, 214–221.

15 N. Arai, N. Saito, H. Nishiyama, Y. Shimodaira, H. Kobayashi, Y. Inoue and K. Sato, *Chem. Lett.*, 2008, **37**, 46–47.

16 A. Dwivedi, H. K. Poswal, R. Shukla, S. Velaga, B. D. Sahoo, V. Grover and M. N. Deo, *High Press. Res.*, 2019, **39**, 17–35.

17 M. El Amrani, V. Ta Phuoc, M. R. Ammar, M. Zaghrioui and F. Gervais, *Solid State Sci.*, 2012, **14**, 1315–1320.

18 P. Hartley, R. G. Egdell, K. H. L. Zhang, M. V. Hohmann, L. F. J. Piper, D. J. Morgan, D. O. Scanlon, B. A. D. Williamson and A. Regoutz, *J. Phys. Chem. C*, 2021, **125**, 6387–6400.

19 Y. Yu, N. Lin, H. Wang, R. Xu, H. Ren and X. Zhao, *RSC Adv.*, 2020, **10**, 4080–4086.

20 M. I. Hussain, R. M. A. Khalil, F. Hussain, M. Imran, A. M. Rana and S. Kim, *Mater. Sci. Semicond. Process.*, 2020, **113**, 105064.

21 K. A. Alrashidi, A. Dixit, A. Nazir, E. A. Khera, S. Mohammad, M. Manzoor, R. Khan and R. Sharma, *J. Inorg. Organomet. Polym.*, 2024, 1–15.

22 T. Degen, M. Sadki, E. Bron, U. König and G. Nénert, *Powder Diffr.*, 2014, **29**, S13–S18.

23 H. Putz, J. C. Schön and M. Jansen, *J. Appl. Crystallogr.*, 1999, **32**, 864–870.

24 V. Pankratov and A. Kotlov, *Nucl. Instrum. Methods Phys. Res.*, 2020, **474**, 35–40.

25 Y. Smortsova, O. Chukova, M. Kirm, V. Nagirnyi, V. Pankratov, A. Kataev and A. Kotlov, *J. Synchrotron Radiat.*, 2025, **32**, 1539–1548.

26 K. Chernenko, A. Kivimäki, R. Pärna, W. Wang, R. Sankari, M. Leandersson, H. Tarawneh, V. Pankratov, M. Kook, E. Kukk, L. Reisberg, S. Urpelainen, T. Käämbre, F. Siewert, G. Gwalt, A. Sokolov, S. Lemke, S. Alimov, J. Knedel, O. Kutz, T. Seliger, M. Valden, M. Hirsimäki, M. Kirm and M. Huttula, *J. Synchrotron Radiat.*, 2021, **28**, 1620–1630.

27 V. Pankratov, R. Pärna, M. Kirm, V. Nagirnyi, E. Nõmmiste, S. Omelkov, S. Vielhauer, K. Chernenko, L. Reisberg, P. Turunen, A. Kivimäki, E. Kukk, M. Valden and M. Huttula, *Radiat. Meas.*, 2019, **121**, 91–98.

28 R. Parna, R. Sankari, E. Kukk, E. Nõmmiste, M. Valden, M. Lastusaari, K. Kooser, K. Kokko, M. Hirsimäki, S. Urpelainen, P. Turunen, A. Kivimäki, V. Pankratov, L. Reisberg, F. Hennies, H. Tarawneh, R. Nyholm and M. Huttula, *Nucl. Instrum. Methods Phys. Res., Sect. A*, 2017, **859**, 83–89.

29 B. Henderson, G. F. Imbusch, B. Henderson and G. F. Imbusch, *Optical Spectroscopy of Inorganic Solids*, Clarendon, Oxford, New York, 1989.

30 N. Srinatha, K. J. Rudresh Kumar, M. R. Suresh Kumar, A. Madhu and B. Angadi, *Ceram. Int.*, 2022, **48**, 3669–3675.

31 N. Srinatha, S. Satyanarayana Reddy, N. Suriyamurthy, K. J. Rudresh Kumar, M. R. Suresh Kumar, A. Madhu and B. Angadi, *Results Opt.*, 2022, **8**, 100242.

32 B. R. R. Krushna, H.-H. Chiu, M.-K. Ho, T.-E. Hsu, B.-L. Lyu, W.-C. Lo, B. Subramanian, K. Manjunatha, S. Y. Wu and H. Nagabhushana, *Mater. Today Sustainability*, 2024, **25**, 100629.

33 S. T. Mukherjee, V. Bedekar, A. Patra, P. U. Sastry and A. K. Tyagi, *J. Alloys Compd.*, 2008, **466**, 493–497.

34 R. Shukla, V. Grover, S. K. Deshpande, D. Jain and A. K. Tyagi, *Inorg. Chem.*, 2013, **52**, 13179–13187.

35 K. Rickert, J. Harris, N. Sedefoglu, H. Kavak, D. Ellis and K. Poeppelmeier, *Crystals*, 2017, **7**, 47.

36 R. S. De Biasi and M. L. N. Grillo, *J. Phys. Chem. Solids*, 2005, **66**, 1806–1809.

37 R. Shendrik, E. Radzhabov, A. Myasnikova, V. Pankratova, A. Šarakovskis, A. Nepomnyashchikh, A. Bogdanov, V. Gavrilenko, E. Kaneva, D. Sofich, T. Garmysheva and V. Pankratov, *Sci. Rep.*, 2025, **15**, 26558.

38 D. Sofich, V. Gavrilenko, V. Pankratova, V. Pankratov, E. Kaneva and R. Shendrik, *Crystals*, 2025, **15**, 489.

39 D. Sofich, A. Myasnikova, A. Bogdanov, V. Pankratova, V. Pankratov, E. Kaneva and R. Shendrik, *Crystals*, 2024, **14**, 500.

40 V. Pankratova, K. Chernenko, D. Bocharov, A. Chesnokov, Y. Sychikova, A. I. Popov and V. Pankratov, *Opt. Mater.*, 2024, **152**, 115554.

41 V. Pankratov, V. Pankratova and A. I. Popov, *Phys. Status Solidi B*, 2022, **259**, 2100475.

42 A. Shalaev, R. Shendrik, A. Rusakov, A. Bogdanov, V. Pankratov, K. Chernenko and A. Myasnikova, *Nucl. Instrum. Methods Phys. Res., Sect. B*, 2020, **467**, 17–20.

43 A. P. Kozlova, V. M. Kasimova, O. A. Buzanov, K. Chernenko, K. Klementiev and V. Pankratov, *Result Phys.*, 2020, **16**, 103002.

44 A. Tuomela, M. Zhang, M. Huttula, S. Sakirzanovas, A. Kareiva, A. I. Popov, A. P. Kozlova, S. A. Aravindh, W. Cao and V. Pankratov, *J. Alloys Compd.*, 2020, **826**, 154205.

45 L. Shirmane and V. Pankratov, *Phys. Status Solidi RRL*, 2016, **10**, 475–479.

46 V. Pankratov, V. Osinniy, A. Kotlov, A. Nylandsted Larsen and B. Bech Nielsen, *Phys. Rev. B: Condens. Matter Mater. Phys.*, 2011, **83**, 045308.

47 P. V. Savchyn, V. V. Vistovskyy, A. S. Pushak, A. S. Voloshinovskii, A. V. Gektin, V. Pankratov and A. I. Popov, *Nucl. Instrum. Methods Phys. Res., Sect. B*, 2012, **274**, 78–82.

48 J. Pejchal, V. Babin, M. Buryi, V. Laguta, F. Hájek, J. Páterek, L. Procházková-Prouzová, L. Havlák, V. Czerneková, V. Vaněček, V. Doležal, J. Havlíček, K. Rubešová, P. Zemenová, A. Falvey, R. Král, V. Pankratov and K. Chernenko, *Mater. Adv.*, 2022, **3**, 3500–3512.

49 Y. Zhydachevskyy, Y. Hizhnyi, S. G. Nedilko, I. Kudryavtseva, V. Pankratov, V. Stasiv, L. Vasylechko, D. Sugak, A. Lushchik, M. Berkowski, A. Suchocki and N. Klyui, *J. Phys. Chem. C*, 2021, **125**, 26698–26710.

50 D. Wang, X. Zhang, X. Wang, Z. Leng, Q. Yang, W. Ji, H. Lin, F. Zeng, C. Li and Z. Su, *Crystals*, 2020, **10**, 1019.

51 X. Wang, Z. Wang, M. Zheng, J. Cui, Y. Yao, L. Cao, M. Zhang, Z. Yang, H. Suo and P. Li, *Dalton Trans.*, 2021, **50**, 311–322.